Insight into the formation of nanostructured MFI sheets and MEL needles driven by molecular recognition

THE JOURNAL OF PHYSICAL CHEMISTRY C

Article

Cite This: J. Phys. Chem. C 2019, 123, 5326−5335

pubs.acs.org/JPCC

Insight into the Formation of Nanostructured MFI Sheets and MEL Needles Driven by Molecular Recognition

Roderigh Y. Rohling,[†] Bartłomiej M. Szyja,[†,‡] and Emiel J. M. Hensen*[,†]

[†]Inorganic Materials Chemistry, Department of Chemical Engineering and Catalysis, Eindhoven University of Technology, Den Dolech 2, 5600 MB Eindhoven, The Netherlands

[‡]Division of Fuels Chemistry and Technology, Faculty of Chemistry, Wrocław University of Science and Technology, Gdańska 7/9, 50-344 Wrocław, Poland

Supporting Information

ABSTRACT: Mesoporous and nanostructured zeolite-based catalysts experience prolonged lifetimes due to increased mass transfer and reduced micropore obstruction by coke formation as compared to their bulky microporous counterparts. Diquaternary ammonium structure-directing agents (SDAs) can be used to synthesize hierarchical MFI sheet-like and MEL needle-like zeolites. An explanation of the underlying molecular-level details of the synthesis of these nanostructured zeolites is presented on the basis of non-covalent interactions between the template and zeolite surfaces as well as silicate oligomers studied by means of classical molecular dynamics. Use was made of Si_{11} and Si_{33} silicate oligomers that contain structural features of the framework to be formed as originally proposed by the Leuven group. Molecular recognition is driven by a combination of strong electrostatic and weaker dispersion interactions. An analysis of the early stage of zeolite formation is necessary, as the template adsorption energies in the fully formed zeolite crystals cannot explain the preferential growth of the MFI sheets or MEL needles. Specifically, it is found that the differences in dispersion interactions between the SDA alkyl chains and the silicate oligomers are decisive in the formation of particular zeolite structures.

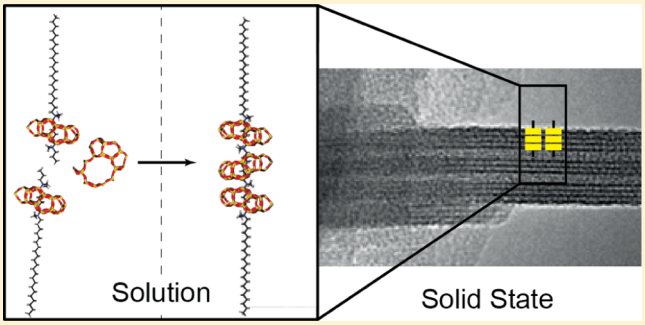

1. INTRODUCTION

Zeolites are crystalline microporous aluminosilicates that play a crucial role in catalysis, sorption, and separation applications. They have a high surface area and exhibit high thermal and chemical stabilities. Their molecular-sized and -shaped micropores endow the embedded strong Brønsted acid sites to convert hydrocarbons and other reactants in a shape-selective manner.[1] More than 200 different zeolite topologies are known to date.[2]

Although synthesizing zeolites might be considered a routine laboratory procedure, many aspects about the formation of zeolites remain ill-understood. One of the important questions relates to the function of structure-directing agents (SDAs), which are usually small organic molecules, used for this purpose.[3] The interactions between the SDA and silicate species result in the formation of specific zeolite topologies via a process that involves nucleation of crystalline domains followed by growth of the zeolite.[4] The exact chain of molecular events that leads to zeolite crystallization continues to be a topic of intense study, e.g., early stage (alumino)silica oligomerization without[5−12] or in[13−22] the presence of a template, zeolite-template interaction,[23−25] and crystallization/growth mechanisms[26−42] (note that these references are not exhaustive). Insight into such molecular phenomena would not only allow improving the synthesis of existing zeolites but also guide the way to new zeolite topologies. A topical area of interest is the synthesis of hierarchically organized zeolites in which additional inter- or intracrystalline pores decrease mass transfer limitations usually encountered in zeolite catalysis, leaving a significant part of the zeolite crystal unused.[43] Hierarchically organized or mesoporous zeolites have been demonstrated to offer superior catalytic activity and extended lifetime as compared to their conventional bulk counterparts.[44−46]

Hierarchically organized zeolites can be obtained by different approaches that have been properly reviewed. These procedures include top-down methods involving the postsynthesis modification of zeolites, or bottom-up methods based on specific interactions of silicate species with a SDA or a combination of SDAs that direct the structure at nano- and mesoscopic levels.[44−48] Of the latter, diquaternary ammonium surfactants ($C_{22}H_{45}$−N$(CH_3)_2$−C_6H_{12}−N$(CH_3)_2$−C_6H_{13}), as first explored by the group of Ryoo, are exemplary.[44,49]

Recently, we have demonstrated by using a combination of small-angle X-ray scattering (SAXS) and electron microscopy that a multilamellar sheet-like morphology of the resulting

Received: August 27, 2018
Revised: February 3, 2019
Published: February 13, 2019

DOI: 10.1021/acs.jpcc.8b08251
J. Phys. Chem. C 2019, 123, 5326−5335

hierarchically organized zeolites is already formed at an early stage of the synthesis, i.e., before crystallization occurs, through specific interactions of silicate species with the head group of the SDA.[49] The ^{29}Si $\{^{1}H\}$ HETCOR NMR measurements evidence that the SDA's head group is already residing in the silicate matrix at this stage of the synthesis, with Raman spectroscopy hinting at the presence of structural motifs of MFI zeolites. These findings illustrate that the SDA impacts the growth of silicate oligomers and organizes the oligomer agglomerates already at an early stage.

From the appearance of a multilamellar phase in the SAXS spectra and the yield of crystalline nanosheets, we inferred that the function of the SDA's hydrophobic tail is to limit the growth of the zeolite in the *b*-direction of the zeolite MFI topology. Molecular modeling further indicated that preferential interactions of silicate precursor structures with the hydrophobic parts close to the quaternary ammonium centers in the $C_{22}H_{45}-N(CH_3)_2-C_6H_{12}-N(CH_3)_2-C_3H_7$ SDA can explain the formation of the anisotropic MFI pore topology. To be specific, presumed ring-like Si_{33} silicate oligomers do not interact with the methyl side chains on the quaternary ammonium centers.[49] This hints at the template being unable to be perpendicularly oriented with respect to a straight MFI pore.

When applying the methyl-based template in the zeolite synthesis, very thin MFI sheets are obtained. By using $C_{22}H_{45}-N(C_3H_7)_2-C_6H_{12}-N(C_3H_7)_2-C_3H_7$, the MEL zeolite is obtained. Upon employing the latter propyl-based SDA, MEL needles are grown whose size in the equivalent *a*- and *b*-directions is limited, although not to the extent of the MFI nanosheets, whereas the growth in the *c*-direction is rapid.

In the present work, we study the formation of MFI nanosheets and MEL nanoneedles (Figure 1a) by expanding our molecular modeling efforts to understand better the molecular interactions between the SDAs and silicate Si_{33} precursors (Figure 1b–e). These precursors also contain structural motifs of the final zeolite crystal (Figure 1e). The SDA directs the formation of MFI nanosheets and MEL nanoneedles by inducing a specific precursor orientation. We want to elucidate which factors govern the formation of MFI nanosheets and MEL nanoneedles when, respectively, methyl-based and propyl-based SDA are used. In our analysis, it is assumed that the kinetics of the Si–O–Si bond formation favor the agglomeration of the Si_{33} precursors. This also implies fast interconversion between the MFI-Si_{33} and MEL-Si_{33} precursors. Eventually, we hypothesize that the relative orientation of these precursors is thus governed by the interaction between both themselves and the template. This is in essence a thermodynamic point of view in which the stability of particular arrangements of templates and precursors or surfaces determines the outcome.[50−55] We emphasize that the used enantiomeric Si_{33} silicate oligomers initially proposed by the Leuven group serve as a conceptual model for a wider range of Si_{10}–Si_{40} oligomers whose size match those of the experimentally observed species that might be involved in the early stages of the formation of nanostructured silicalite-1 and silicalite-2.[26,28,56−58] The Leuven hypothesis suggests that the Si_{33} precursors lead up to the full zeolite crystal upon agglomeration and condensation.[56,59] As we will show below, this approach connects the earlier theoretical work on the formation of bulk MFI or MEL frameworks[14,60] and their nanostructured counterparts.[49] The identified stable configurations can be considered intermediates in the formation of specific zeolite nanostructures. The interactions between the SDAs and silicates are analyzed in detail to obtain the relative contributions of electrostatic and dispersion interactions.

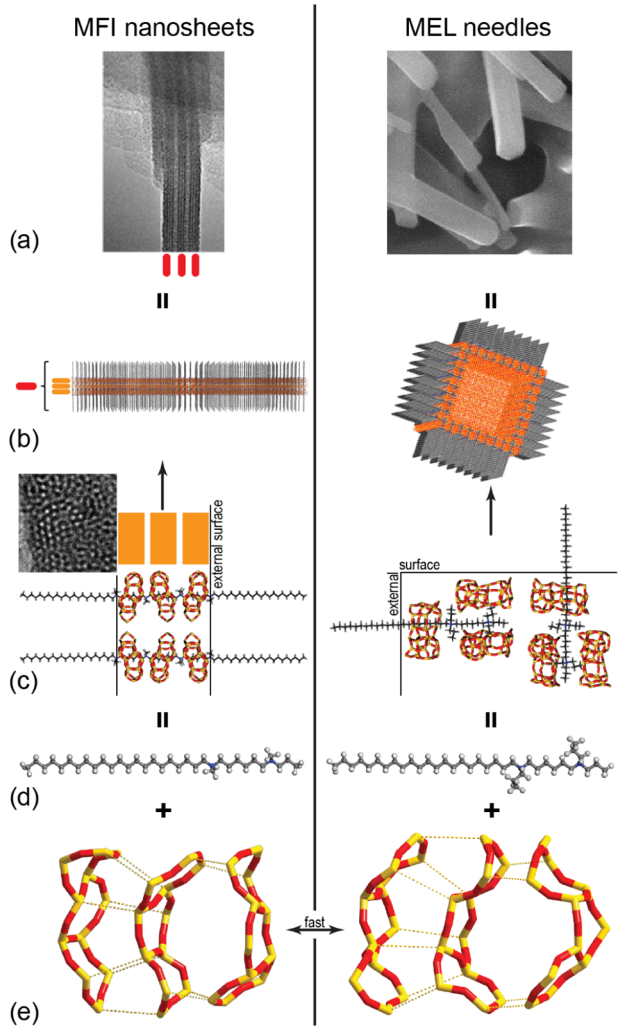

Figure 1. Schematic representation of the mechanism of MFI nanosheet and MEL nanoneedle formation. (a) On the left and right, the MFI nanosheet and MEL needles, respectively. (b) How both MFI (left) and MEL (right) surfaces are terminated with their respective SDAs ($C_{22}H_{45}-N(C_1H_3)_2-C_6H_{12}-N(C_1H_3)_2-C_3H_7$ and $C_{22}H_{45}-N(C_3H_7)_2-C_6H_{12}-N(C_3H_7)_2-C_3H_7$, respectively), and the transmission electron microscopy image illustrates the irregular ordering or presumed MFI-Si_{33}-precursors. (c) Schematic representation of the organization of the SDAs (d) and Si_{33} precursors (e) containing structural motifs of either the MFI or MEL zeolite. Interconversion between two different Si_{33} precursors is assumed to be fast.

2. COMPUTATIONAL DETAILS

The two different Si_{33} precursors used in this work are MFI-Si_{33} and MEL-Si_{33}, which differ in the manner the undecamers (Si_{11}) have trimerized. The undecamer on the right-hand side of the Si_{33} precursor is rotated 180° such that the MFI-Si_{33} (Figure 1e left) contains five-membered rings only, whereas MEL-Si_{33} (Figure 1e right) also contains a four- and six-membered ring. The diquaternary ammonium-based templates consisted of a long "tail" (C_{22}), "linker" (C_6), and "head" (C_3 or C_6). The C_3-terminated SDA had either methyl or propyl side chains. Their structural formulae are $C_{22}H_{45}-N(C_1H_3)_2-$

DOI: 10.1021/acs.jpcc.8b08251
J. Phys. Chem. C 2019, 123, 5326−5335

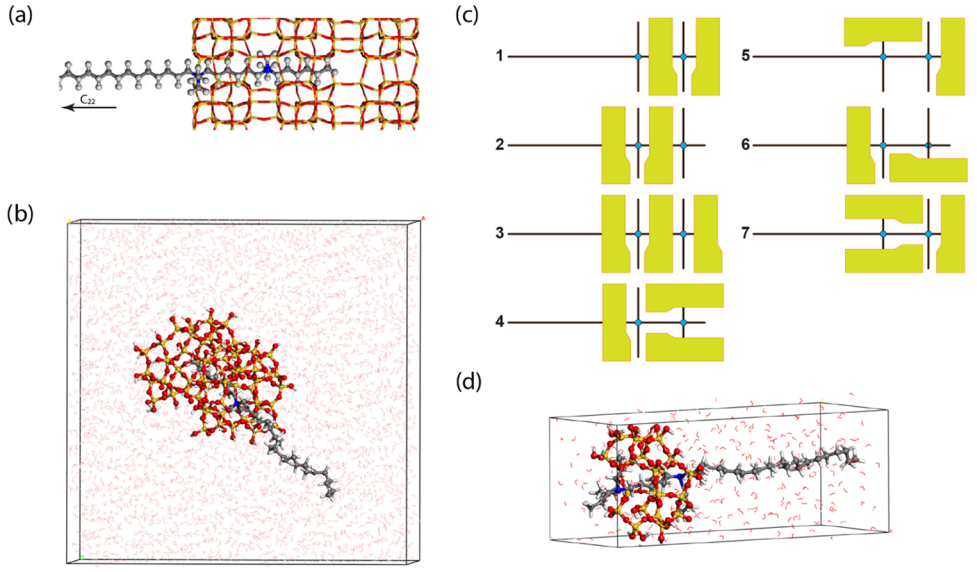

Figure 2. Panel (a) illustrates how a SDA can be embedded in the zeolite structure and panel (b) shows an example of a periodic cell used to study the precursor−template interactions. The relative orientation of the *L*- and *R*-Si_{33} precursors as represented by the yellow blocks in panel (c). Note the thicker parts on every block represents the Si_{22} segment made up of double pentasil rings. The SDAs are shown by brown lines in which the blue dots indicate the ammonium groups. For the sake of conciseness, we refer to the text for an explanation of structures **1**−**7**. The periodic box in (d) was used to simulate the undecamer−template interactions.

$C_6H_{12}-N(C_1H_3)_2-C_6H_{13}$, $C_{22}H_{45}-N(C_1H_3)_2-C_6H_{12}-N(C_1H_3)_2-C_3H_7$, and $C_{22}H_{45}-N(C_3H_7)_2-C_6H_{12}-N(C_3H_7)_2-C_3H_7$. The second and third template are referred to as the methyl- and propyl-based template or SDA, respectively (Figure 1d left and right, respectively). When the SDA is embedded in either the MFI or MEL surface, one of the ammonium groups sticks in the subsurface channel intersection and the other resides at the surface (Figure 2a).

Template−Surface Models. The models consisted of SDAs embedded in MFI and MEL surfaces. Geometry optimizations were performed using Materials Studio 6.0 using the COMPASS forcefield in the Forcite+ module to determine the SDA−zeolite interaction energies. The two cationic charges of each template were balanced by deprotonation of two surface silanol groups. The exact effect of their position was not thoroughly analyzed, but deprotonated silanol groups were consistently located near different templates such that a qualitative trend can be established. We also assumed a defect-free zeolite such that no silanol nests or deprotonated silanol groups were present within the zeolite.

Whereas MFI contains straight and zigzag channels in the [010] and [100] directions, respectively, the MEL framework only has straight channels in the symmetrically identical [100] and [010] directions. Accordingly, we constructed the MFI surfaces exposing either the [100] or the [010] surface and only one MEL surface. Periodic boundary conditions (PBC) were imposed on the system and a vacuum layer of 60 Å separated the zeolite external surfaces from their periodic images in the *z*-direction.

Template−Precursor Agglomerate Models. Large periodic boxes with dimension of 50 Å in all three directions and with explicit water molecules were constructed to study both the interaction of the precursors with the SDAs and the stability of the precursor−SDA complexes in an aqueous environment. The model of the silicate agglomerates consisted of two or three Si_{33} precursors, one SDA and 4000 water molecules (Figure 2b). Special care was again taken to properly charge deprotonated silanol groups located on the precursors complementary to the automated forcefield charge assignment (see the Supporting Information). Models containing a third precursor also contained a free proton to balance the resulting excess −1 charge. This proton resulted in the formation of a hydronium ion by electrostatically coordinating to a water molecule. Despite the experimental synthesis conditions being basic, thus formally making the use of a proton less realistic, this approach allowed us to consistently focus on the interactions between a single template molecule and the Si_{33} precursors. A thorough screening to deduce the energetic effect of varying the position of the deprotonated silanol group was not performed. We note that due to the presence of two ammonium groups, a relatively short-range cation−anion interaction can always be established. Furthermore, due to the spherical shape of the precursors, we expected that the majority of other potential deprotonated silanol sites were essentially replicates of the one we used now. We expect some variations in the magnitude of these ionic interactions as function of the position of the deprotonated silanol group on the precursor. However, despite the experimental synthesis gel being highly basic, and containing many other charged species like other templates and mineralizing agents, thus resulting in potentially short screening lengths, we think that the close proximity of the Si_{33} precursor to the template allows for strong interactions. To facilitate a consistent interpretation of the data, we decided to use the same position in all cases.

The analyzed template−SDA geometries are schematically depicted in Figure 2c. As there are no data available on reasonable starting configurations, we used chemical intuition to create the most likely structures. Briefly, the structures consisted of the template interacting with the *L*- and *R*-enantiomers of either the MFI or MEL precursors.[60] In MFI-, *L*-, and *R*-precursors alternate along the *b*-axis and form a straight channel (**1**−**3**). For consistency, *L*- and *R*−MEL-precursors have also been placed according to structures **1**−**3**. Additionally, for both MFI and MEL type precursors, one *L*-

DOI: 10.1021/acs.jpcc.8b08251
J. Phys. Chem. C 2019, 123, 5326−5335

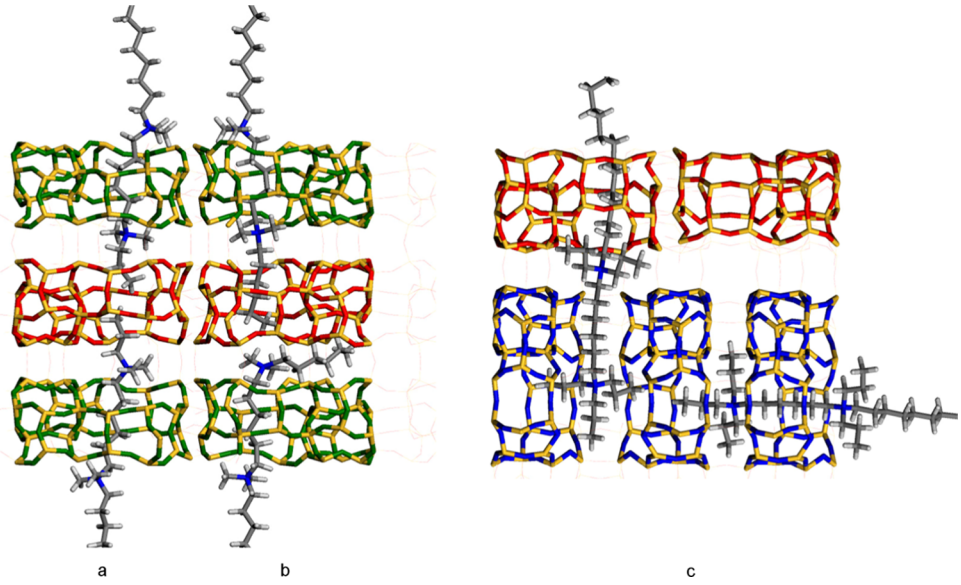

Figure 3. Fit of the SDAs in the Si_{33} precursor complexes, having the same structural features as in the fully formed frameworks. The figure shows the best arrangement of the terminal C_3 chains in MFI (a) and shows the repulsion of the C_6 chains in panel (b). The structure in panel (c) shows the perpendicular orientation of the long chains possible in MEL due to the symmetry of this structure. The oxygen atoms are shown in green, red, and blue to denote different precursors. Silicon, carbon, nitrogen, and hydrogen are shown in yellow, gray, blue, and white, respectively.

and one *R*-precursor were placed opposite and perpendicular to each other with their 10-MR aligned to the template's axis, capped by another template with its 10-MR aligned along the template axis (**4**). Although the overall structure and energetics are not affected by the perpendicular orientation of the precursors due to mirror symmetry, we consistently used the same enantiomer for all simulations. Structure **4** was used to derive structures **5** and **6**. An inverse structure of **4** was used to obtain structure **7**. Additionally, we modeled the MEL(I) and MEL(II) channel intersections.[24]

The Forcite+ module and the COMPASS forcefield were used again for all molecular dynamics (MD) simulations to be consistent with the surface investigations. The systems were pre-equilibrated (NPT-ensemble, 65 ps, 1 bar, 298 K) using the Berendsen and Nosé baro- and thermostat, respectively. A typical production run was performed using the NVT-ensemble for 600 ps at 298 K using the Nosé thermostat. All runs were performed with a time step of 1 fs and a 12.5 Å cutoff distance for both van der Waals nonbonded and electrostatic interactions using atom-based summation methods.

The COMPASS forcefield was designed for condensed phase simulations (common organic molecules, common polymers, and small gas molecules) and the parameters have been derived using high-level ab initio calculations and molecular dynamic simulations.[61−66] The parameters are optimized to fit the experimental data of both gaseous and condensed phases. The version used in our work also contains parameters for inorganic materials including metals, metal oxides, metal halides, and zeolites.[67,68] The most significant difference between these parameters and those used for organic molecules is that the temperature effect has not been considered for the inorganic materials. That is, parameterization and validations are based on zero temperature energy minimization calculations instead of finite-temperature MD simulations.

The trajectories were analyzed with a PERL script (Scripting module) to calculate the potential and interaction energies of the system after the removal of all water molecules in each trajectory step. The interaction energies are computed between the template and the precursor of interest in the absence of other precursor(s) by referencing the two-body system against their isolated gas phase mimics. This allowed us to have the averaged models suitable for the interaction energy analysis with geometries dependent on the reaction environment. These energies have been calculated for the most representative parts of the trajectories based on the stability criterion, i.e., for a sufficiently long section of the run where the geometry did not significantly change. The length of this period was an arbitrary assumption but typically was 150 ps or longer.

Template−Undecamer Agglomerate Models. Both the methyl- and propyl-based templates were each put in a box with dimensions of 15 × 15 × 40 $Å^3$ (PBC, 300 H_2O), mimicking a condensed phase by allowing the undecamers and template to interact with their periodic images (Figure 2d). The computational procedure consisted of 40 ps NPT equilibration (298 K, 1 bar) and a 300 ps NVT production run (298 K). The simulation box is shown in Figure 2d. Similar settings as for the template−precursor agglomerate models were used.

Interaction Energy Deconvolution. An infinite hydrocarbon chain going through the 10-MR channel of the precursor was created to estimate the contribution of the dispersion interactions of the alkyl groups of the SDA to the overall interaction energy. Infinite length was obtained using PBC. On the basis of this model, we expect to obtain a reasonable estimate of different contributions to the interaction energy independent of the molecular geometries or chemical surroundings. The channel of the precursor is essentially the 10-membered ring that eventually forms the 10-membered ring micropore upon condensation of the precursors. An ammonium group with methyl or propyl side group was subsequently added to the infinite carbon chain, accounting for the interaction of the side group with the precursors. The electrostatic contributions were determined by replacing the SDA from one of the trajectories with two NH_4 molecules,

DOI: 10.1021/acs.jpcc.8b08251
J. Phys. Chem. C 2019, 123, 5326−5335

whose nitrogen atoms were located at exactly the same positions as the nitrogen atoms in the SDA.

3. RESULTS AND DISCUSSION

3.1. SDA−Crystal Surface Interactions. The experimental results reported on MFI nanosheets indicate that the MFI[010] surface is predominantly expressed.[44,49] This is hypothesized to be due to limited zeolite growth in the *b*-direction of the MFI topology. This phenomenon, in turn, is thought to result from the preferential location of the SDA along the straight channels blocking further growth by the presence of the C_{22} tail. To test this hypothesis, the interaction energies (E_{int}) of three different templates, embedded in the MFI and MEL zeolite frameworks as shown in Figure 3, are listed in Table 1. These data provide an insight into the relative stability of the different templates located at various positions.

Table 1. Interaction Energies (kJ/mol) of the SDAs Inside the Pores of MFI and MEL Sheets[a]

	propyl	methyl		methyl	
	$C_{22\text{-}6\text{-}3l}$	$C_{22\text{-}6\text{-}3l}$	$C_{22\text{-}6\text{-}3b}$	$C_{22\text{-}6\text{-}6l}$	$C_{22\text{-}6\text{-}6b}$
MFI[010]	−519	−569	−553	−603	−607
MFI[100]	−662	−586	−595	−611	−620
MEL[100]	−532	−548	−553	−603	−595

[a]Templates were embedded in either a linear (l) or bent (b) fashion.

The analysis is based on the underlying assumption that the kinetics of the Si−O−Si bond formation favors the agglomeration of the Si_{33} precursors. This assumption also implies that the interconversion between the MFI-Si_{33} and MEL-Si_{33} precursors is fast. The relative orientation of these precursors is thus achieved by the interaction between both themselves and the template. This is in essence a thermodynamic point of view in which the stability of particular arrangements of templates and precursors or surfaces determines the outcome.

Linearly embedded methyl-based $C_{22\text{-}6\text{-}3}$ and $C_{22\text{-}6\text{-}6}$ in MFI[010] are, respectively, 17 and 8 kJ/mol less stable than that in MFI[100]. When the terminal C_3 or C_6 head groups are bent, so that they occupy the channels perpendicular to the axis of the template (Figure 3b), we find marginal differences as compared to their fully linear counterparts ($\Delta E_{int,max}$ = 13 kJ/mol for MFI[010]). This comparison shows that there should be no preferential expression of either the MFI[100] or MFI[010] surface when methyl-based templates are used. This finding contradicts the experimental findings of the predominantly expressed MFI[010] surface.

As it is experimentally found that the propyl-based SDA yields MEL nanoneedles,[49] we compared the energies of this SDA located in MFI[100] and MEL[100]. The interaction energy of the propyl-terminated $C_{22\text{-}6\text{-}3}$ with MFI[100] is 130 kJ/mol stronger than that terminated with MEL[100]. This means that the propyl-based templates should predominantly yield the MFI framework type. The results are thus also inconsistent with the experiments.

As none of the interaction energies with the fully formed surfaces can clearly explain the formation of either MFI or MEL zeolite nanostructures, we conclude that the main templating effect must be present in an even earlier stage of the zeolite synthesis.

3.2. SDA Interactions with MFI- and MEL-Si_{33} Precursors. We used the Si_{33} precursors proposed by the Leuven group[56,59] to conceptually understand the structure directing behavior of $C_{22\text{-}6\text{-}3}$ SDAs, whose close proximity and interaction with silicate species on the micro- and mesoscale during the early stages of zeolite formation has been suggested.[49] We employed molecular dynamics to capture the characteristics of the complex solvent environment to study the role of the SDA on Si_{33} precursor agglomeration. The interaction of both methyl- and propyl-based templates with the MFI- and MEL-Si_{33} precursors was studied.

The density in the periodic cell was determined to be 1 ± 0.01 g/cm^3. As the Si_{33} precursors are already formed in the low-temperature polycondensation process of tetraethyl orthosilicate,[26] the obtained system densities are considered reasonable. It should be noted that our simulations deal with the early stage of zeolite synthesis, which is experimentally initiated at ambient conditions. The chemical composition in our simulations are in reasonable agreement with the one used in our previous experimental work.[49] Experimentally, the ratio is 9SDA:100SiO_2:4000H_2O. In the current work, the ratio is 1SDA:ca. 66−99SiO_2:4000H_2O. We consider our work to reflect the low-SDA-density regime, especially since these surfactants can easily form micelles or bilayers reducing the actual free SDA concentration in a solution.

The results of the molecular dynamics simulations are shown in Figure 4. The interaction energies are displayed in Figure 4a, and MEL-7 on propyl- and methyl-based SDA is depicted in Figure 4b,c, respectively. It is noted that the value of MEL coordination to the N^2 position on the propyl-based template in Figure 4 is not as thoroughly sampled as the other

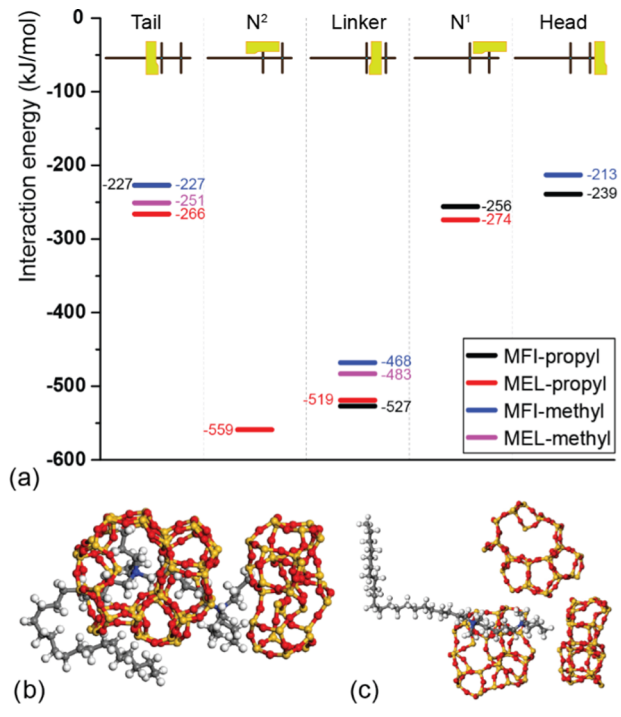

Figure 4. Graphical representation of the interaction energies of the precursors coordinated to different locations on $C_{22\text{-}6\text{-}3}$ templates (a). When no value is reported for a specific location, then the structure was found not to be stable. Snapshots of the final geometries of structures MEL-7 on the propyl- and methyl-based SDAs are shown in (b) and (c), respectively. Water molecules are not drawn.

DOI: 10.1021/acs.jpcc.8b08251
J. Phys. Chem. C 2019, 123, 5326−5335

positions. The other interaction energies are obtained by averaging over four to seven runs. The results indicate that the MFI-Si_{33} precursor located on the C_6 linker is at least twice as stable as that located on the C_3 head group (e.g., $\Delta E_{int,linker\text{-}head}$ = −255 and −288 kJ/mol on the C_6 linker of methyl- and propyl-based SDAs, respectively). Additionally, MFI-Si_{33} positioned on the C_3 head group is as stable as that positioned on the C_{22} tail ($\Delta E_{int,tail\text{-}head}$ = −14 and −12 kJ/mol for methyl- and propyl-based SDA, respectively). The all-side-on-coordinated MFI-Si_{33} with the 10-MR aligned perpendicularly to the methyl-based template's axis collapsed (similar to Figure 4c). This collapse was characterized by the closure of the 10-MR by the loss of structural rigidity of the Si_{11} segment.

Upon comparing the methyl- and propyl-based SDA, only a terminal ammonium group on the propyl-based template was found to be a stable site for side-on-coordinated MFI-Si_{33} ($\Delta E_{int,tail\text{-}N1}$ = 29 kJ/mol). For MEL-Si_{33}, this picture does not change qualitatively, although the stability is generally increased ($\Delta E_{int,tail\text{-}N1}$ = 8 kJ/mol) as evidenced by the larger interaction energies. An example of the reason for terminal ammonium group on the propyl-based SDA being a stable coordination side is shown in Figure 4b. That is, in addition to ionic interactions, the dispersion interactions between the precursors and the propyl groups keep the precursor in place.

Summarizing, side-on coordination of the Si_{33} precursors is not possible on the methyl-based template. The precursors are predicted to only form along the template's axis, with the template going through the 10-MR ring. For the propyl-based template, side-on coordination is possible and results in stable structures. The MEL precursors are aligned such that the MEL zeolite can be formed.

3.3. Precursor Organization near the Templates. To understand the preferred coordination of both precursor types on the C_6-linker position, we deconvoluted the interaction energy into dispersive and electrostatic components. This was done by a systematic study of simplified models mimicking the SDA−precursor complex (Figure 5). The results are summarized in Table 2. The main contributor to the interaction energy is the electrostatic component, which is twice as high as the dispersion interactions (about 190 and 90 kJ/mol, respectively). The two different side groups (methyl or propyl, Figure 5b,c, respectively) provide different degrees of stabilization, depending on the chain length and the type of Si_{33} precursor. When MFI-Si_{33} is located on the linker, the four propyl side groups provide stronger stabilization via dispersion interactions than the four methyl side groups (ΔE_{int} = −46 kJ/mol). For MEL-Si_{33}, the interaction with the side groups is generally stronger than that for MFI-Si_{33} (ΔE_{int} = −20 kJ/mol). However, the relative difference between methyl and propyl remains identical. This analysis thus explains that the tail and head positions are only half as stable as the linker position because the Si_{33} precursors at those positions only interact with one ammonium group and only two alkyl side groups.

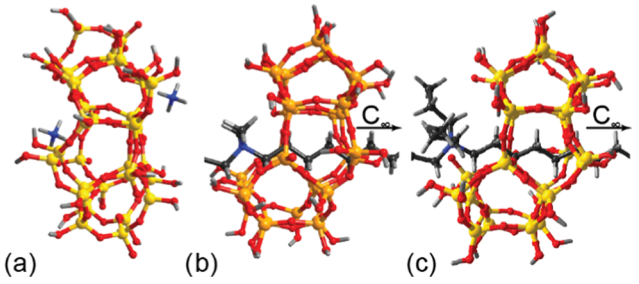

Figure 5. Examples and snapshots of geometries used to deconvolute the interaction energy into the dispersion and electrostatic components. (a) Two ammonia molecules at exactly the same location as the ammonium basis in the methyl-based $C_{22\text{-}6\text{-}3}$ template. (b) A MEL precursor on the infinite hydrocarbon chain including the ammonium group and two methyl groups. (c) Similar to (b) but with propyl side groups.

Table 2. Deconvolution of the Interaction Energy in Dispersion and Electrostatic Contributions

interaction type	topology	E_{int} (kJ/mol)
dispersion interaction—C−$C_{backbone}$	MEL	−92
	MFI	−92
dispersion interaction—2 propyl side groups	MEL	−84
	MFI	−64
dispersion interaction—2 methyl side groups	MEL	−61
	MFI	−41
N^+ electrostatic contribution—both N^+	MEL	−379
	MFI	−385
N^+ electrostatic contribution—single N^+	MEL	−189
	MFI	−193

We envisage that for higher local SDA concentration, a precursor can be stabilized at the head group with the aid of a second template. In this configuration, two ammonium bases flank the precursor too, each belonging to another SDA, reminiscent of the situation in Figure 3a. The precursors are then still aligned according to the MFI precursor stacking scheme and the thickness matches that of the experimentally obtained MFI sheets. Ryoo and co-workers observed an increasing nanosheet thickness upon a concomitant increase in ammonium bases per template.[69] In line with our reasoning, they also observed that the ammonium group linked to the tail had no structure-directing role.

The energy deconvolution also explains the lack of stability of the precursors on the methyl side groups. Short methyl groups cannot penetrate into the 10-MR channel of the precursor and can therefore not provide the necessary stabilization.[15] The electrostatic interaction with the quaternary ammonium group is the main contributor to the interaction energy in such a coordination complex. However, electrostatic interactions are long range and independent of direction. This means that they will not induce a particular orientation of the precursors with respect to each other. In contrast, alkyl side groups will do so by imposing steric constraints and interacting with the precursors via dispersion interactions. We note that under practical synthesis conditions, the typical pH is about 10−13 in the early stage of synthesis, depending on the type of zeolite to be synthesized.[36,70] Such a high pH will cause significant screening of the cationic charge on the ammonium groups. Nevertheless, upon formation of the tightly bound precursor−template coordination complex, still no structure-directing effects are expected from the ionic interactions between the template and the precursor. It can thus be concluded that the dispersion interactions play an essential role in precursor alignment.

From the above analysis, we tentatively propose that the Si_{33} precursor preferentially forms around the alkyl linker. Consequently, steric effects due to the size of the Si_{33} precursors would then prevent a perpendicular stacking of

DOI: 10.1021/acs.jpcc.8b08251
J. Phys. Chem. C 2019, 123, 5326−5335

precursors once the alkyl linker is occupied. Then, only the parallel precursor stacking scheme along the axis of the SDA is left.

In our previous work, MEL needles were found to be thicker than MFI nanosheets.[49] This implies that propyl-based SDA is not as effective in limiting the MEL nanoneedle growth in the *a*- and *b*-direction as compared to methyl-based SDA for limiting the MFI nanosheet growth in the *b*-direction. It is possible that some amount of propyl-based SDA is incorporated in the growth of MEL nanoneedle. For instance, upon comparing MFI and MEL precursors on methyl- and propyl-based templates organized according to structure **7**, respectively (Figure 4b,c), we find that the supramolecular assemblies for the MFI case are not stable. For the MEL case, the C_{22} tail curls around the Si_{33} precursors. This is ascribed to favorable dispersion interactions between template and precursors. The silicate agglomerate remains intact during the simulations. Furthermore, Meng et al.[71] reported an increase in ZSM-5 crystallinity with increasing amount of cetyltrimethylammonium incorporated in the growing zeolite. As the MEL needles are highly crystalline, as evidenced by the very sharp X-ray diffraction peaks,[49] we hypothesize that a significant portion of the propyl-based SDA should thus be embedded in the growing MEL zeolite. This is possible because the C_{22} tail has a lot of conformational freedom. This might be beneficial for the formation of the MEL zeolite because the MEL2 intersection is characterized by a large distance between the pore axes at the intersection[24] and the flexible C_{22} tail could thus provide stabilization via dispersion interactions with the siliceous framework. Yet, despite the propyl-based SDA being incorporated in the MEL zeolite, we see a substantial morphological difference between the commonly synthesized MEL zeolite cystals[72−74] and the MEL nanoneedles in our previous work.[49] So, although an amount of the propyl-based SDA is incorporated in the growing crystal, the SDA is still likely to act as an *a*- and *b*-direction growth retardant and, especially, induces the formation of distinct needles and large mesoporous voids.

3.4. Formation of Precursor. The relative stability of the precursors is not the only important factor in deciding whether MFI- or MEL-based zeolite frameworks are formed. The ease with which the precursors form should be considered as well. A theoretical study on TPA^+- and TBA^+-mediated precursor formation has demonstrated how the precursor forms around these tetra-alkyl ammonium species.[14] This process involves the displacement of the ammonium group, which is initially located within the nascent 10-MR channel. Upon increasing the condensation of the 10-MR channel, TPA^+ moves away and positions next to the 10-MR channel with only the alkyl groups stabilizing it.

Using NMR techniques, it has been shown that methyl-based $C_{22\text{-}6\text{-}3}$ SDA already resides in the silica matrix at the early stage of MFI nanosheet synthesis.[49] An extrapolation of the precursor formation concept near the tetra-alkyl ammonium cations to that of the designer SDAs thus seems chemically intuitive.

Whereas the precursor formation concept seems readily applicable to the C_3 head group in $C_{22\text{-}6\text{-}3}$, it is less straightforward for the C_6 linker that connects both ammonium bases. The C_6-linker position is the most stable position for a precursor to be formed, but its highly constrained and hindered environment provides less freedom for the undecamers and precursors to adopt this position. This is especially the case for the propyl-based SDA.

The effect of steric hindrance imposed by the alkyl side groups near the C_6-linker was investigated by modeling systems with two undecamers capable of forming the 10-MR upon condensation. We used both the propyl- and methyl-based $C_{22\text{-}6\text{-}3}$ to be able to establish differences. The initial state of both the methyl- and propyl-based $C_{22\text{-}6\text{-}3}$ are shown in Figure 6a,c, respectively. The respective final states, obtained after equilibration and production runs, are shown in Figure 6b,d.

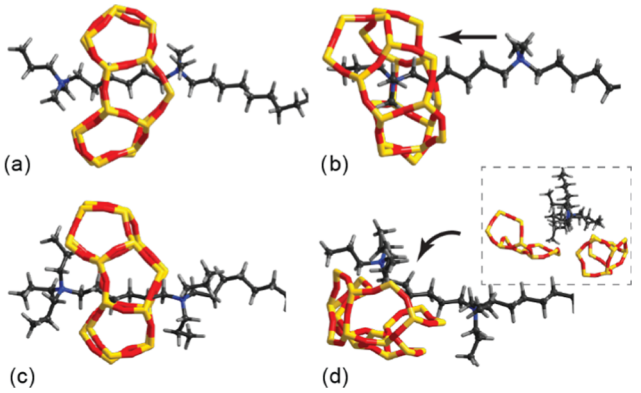

Figure 6. Snapshots of the trajectories of the double undecamer systems around the linker of a methyl-based (a, b) and propyl-based (c, d) templates at the start (a, c) and end (b, d) of the trajectory. The arrows indicate the movement of the undecamers with respect to their initial position. The inset in (d) shows the front view of (d).

For the methyl-based SDA, the undecamers coordinate preferentially to the ammonium base before condensation takes place. This is similar to the initial state found for the study on TPA^+-mediated precursor formation. Thus, upon condensation, the undecamers may move to the C_6 linker, which provides stabilization via dispersion interactions, reminiscent of Figure 6a. Meanwhile, the two ammonium groups are located on both sides of the undecamers for maximum electrostatic interactions. Consequently, new precursors can only stack parallel with the template going through the 10-MR of all precursors.

For the propyl-based SDA, the undecamers displace and reorient from the C_6 linker to one of the alkyl side chains. In doing so, they lose their perpendicular orientation with respect to the template's axis via a combination of rotation and lateral translation. The result is a parallel orientation. Condensation at this position would favor the formation of a side-on-coordinated precursor. When this happens, the typical MEL stacking configurations, as shown in Figure 2c, entries **4**−**7**, become available. Such supramolecular assemblies could give rise to the formation of the MEL structure. We note, though, that due to the small size of the simulation box, the observed configuration might not be the true configuration found under practical synthesis conditions. Yet, the observation that steric hindrance and crowding causes the undecamers to move near the propyl-based template remains undoubtedly valid.

4. CONCLUSIONS

We have given an explanation on the molecular recognition-driven formation of MFI nanosheets and MEL nanoneedles. Although electrostatic interactions have a dominant contribu-

DOI: 10.1021/acs.jpcc.8b08251
J. Phys. Chem. C 2019, 123, 5326−5335

tion to the total interaction energy, dispersion interactions play a critical role in both the stability and coordination of the precursors to the diquaternary ammonium templates. Side-on-coordinated MFI-Si_{33} on methyl-based SDAs are unstable due to weak interactions with the methyl side groups. The precursors are subject to migration and a collapse of the MFI- and MEL-Si_{33} units was observed. The formation of the precursor on the C_6 linker of a methyl-based diquaternary ammonium template is not blocked and leads to an energetically stable system. Parallel stacking is thus the only reasonable formation scheme on a methyl-based SDA, eventually leading up to MFI zeolite formation. A propyl-based SDA, on the other hand, can stabilize the side-on-coordinated precursors. The formation of the central precursor on the linker of these propyl-based templates is significantly more difficult, as it is severely hindered by the propyl side groups. Rotation around the tripropylammonium head group allows a precursor to adopt a side-on coordination with a favorable coordination. These are both dispersive and electrostatic in nature. Stacking is thus less likely to occur and the results are in favor of the perpendicular stacking mechanism for MEL-Si_{33}.

■ ASSOCIATED CONTENT

Supporting Information

The Supporting Information is available free of charge on the ACS Publications website at DOI: 10.1021/acs.jpcc.8b08251.

Forcefield charge adjustment procedure for deprotonated silanol groups (PDF)

■ AUTHOR INFORMATION

Corresponding Author

*E-mail: e.j.m.hensen@tue.nl

ORCID

Emiel J. M. Hensen: 0000-0002-9754-2417

Notes

The authors declare no competing financial interest.

■ ACKNOWLEDGMENTS

This work was partially supported by the Netherlands Center for Multiscale Catalytic Energy Conversion (MCEC), an NWO Gravitation programme funded by the Ministry of Education, Culture and Science of the government of the Netherlands. B.M.S. would like to acknowledge the financial support from the Polish Ministry of Higher Education for statutory activity subsidy for the Faculty of Chemistry of Wrocław University of Science and Technology for year 2018.

■ REFERENCES

(1) Cundy, C. S.; Cox, P. A. The Hydrothermal Synthesis of Zeolites: History and Development from the Earliest Days to the Present Time. *Chem. Rev.* **2003**, *103*, 663−701.

(2) Baerlocher, Ch.; McCusker, L. B. Database of Zeolite Structures. http://www.iza-structure.org/databases/ (accessed 22, Nov, 2018).

(3) Subotić, B.; Bronić, J. In *Handbook of Zeolite Science and Technology*; Auerbach, S. M., Carrado, K. A., Dutta, P. K., Eds.; Dekker: Basel, 2003; 129−203.

(4) Cundy, C. S.; Cox, P. A. The Hydrothermal Synthesis of Zeolites: Precursors, Intermediates and Reaction Mechanism. *Microporous Mesoporous Mater.* **2005**, *82*, 1−78.

(5) Rao, N.; Gelb, L. Molecular Dynamics Simulation of the Polymerization of Aqueous Silicic Acid and Analysis of the Effects of Concentration on Silica Polymorph Distributions, Growth Mechanisms and Recation Kinetics. *J. Phys. Chem. B* **2004**, *108*, 12418−12428.

(6) Trinh, T. T.; Jansen, A. P. J.; Van Santen, R. A. Mechanism of Oligomerization Reactions of Silica. *J. Phys. Chem. B* **2006**, *110*, 23099−23106.

(7) Trinh, T. T.; Jansen, A. P. J.; Van Santen, R. A.; Meijer, E. J. Role of Water in Silica Oligomerization. *J. Phys. Chem. C* **2009**, *113*, 2647−2652.

(8) Pelster, S. A.; Kalamajka, R.; Schrader, W.; Schüth, F. Monitoring the Nucleation of Zeolites by Mass Spectrometry. *Angew. Chem., Int. Ed.* **2007**, *46*, 2299−2302.

(9) Malani, A.; Auerbach, S. M.; Monson, P. A. Probing the Mechanism of Silica Polymerization at Ambient Temperatures Using Monte Carlo Simulations. *J. Phys. Chem. Lett.* **2010**, *1*, 3219−3224.

(10) Pereira, J. C. G.; Catlow, C. R. A.; Price, G. D. Ab Initio Studies of Silica-Based Clusters. Part I. Energies and Conformations of Simple Clusters. *J. Phys. Chem. A* **1999**, *103*, 3252−3267.

(11) Yang, C. S.; Mora-Fonz, J. M.; Catlow, C. R. A. Stability and Structures of Aluminosilicate Clusters. *J. Phys. Chem. C* **2011**, *115*, 24102−24114.

(12) Yang, C.-S.; Mora-Fonz, J. M.; Catlow, C. R. A. Modeling the Polymerization of Aluminosilicate Clusters. *J. Phys. Chem. C* **2012**, *116*, 22121−22128.

(13) Szyja, B. M.; Vassilev, P.; Trinh, T. T.; Van Santen, R. A.; Hensen, E. J. M. The Relative Stability of Zeolite Precursor Tetraalkylammonium-Silicate Oligomer Complexes. *Microporous Mesoporous Mater.* **2011**, *146*, 82−87.

(14) Szyja, B.; Jansen, A.; Verstraelen, T.; Van Santen, R. Molecular Dynamics Study of the silica−water−SDA Interactions. *Phys. Chem. Chem. Phys.* **2009**, *11*, 7605.

(15) Verstraelen, T.; Szyja, B. M.; Lesthaeghe, D.; Declerck, R.; Van Speybroeck, V.; Waroquier, M.; Jansen, A. P. J.; Aerts, A.; Follens, L. R. A.; Martens, J. A.; et al. Multi-Level Modeling of Silica-Template Interactions during Initial Stages of Zeolite Synthesis. *Top. Catal.* **2009**, *52*, 1261−1271.

(16) Trinh, T. T.; Rozanska, X.; Delbecq, F.; Sautet, P. The Initial Step of Silicate versus Aluminosilicate Formation in Zeolite Synthesis: A Reaction Mechanism in Water with a Tetrapropylammonium Template. *Phys. Chem. Chem. Phys.* **2012**, *14*, 3369−3380.

(17) Jin, L.; Auerbach, S. M.; Monson, P. A. Simulating the Formation of Surfactant-Templated Mesoporous Silica Materials: A Model with Both Surfactant Self-Assembly and Silica Polymerization. *Langmuir* **2013**, *29*, 766−780.

(18) Catlow, C. R. A.; Coombes, D. S.; Lewis, D. W.; Pereira, J. C. G. Computer Modeling of Nucleation, Growth, and Templating in Hydrothermal Synthesis. *Chem. Mater.* **1998**, *10*, 3249−3265.

(19) Burkett, S. L.; Davis, M. E. Mechanism of Structure Direction in the Synthesis of Si-ZSM-5: An Investigation by Intermolecular 1H-29Si CP MAS NMR. *J. Phys. Chem.* **1994**, *98*, 4647−4653.

(20) Burkett, S. L.; Davis, M. E. Mechanisms of Structure Direction in the Synthesis of Pure-Silica Zeolites. 1. Synthesis of TPA/Si-ZSM-5. *Chem. Mater.* **1995**, *7*, 920−928.

(21) Fyfe, C. A.; Darton, R. J.; Schneider, C.; Scheffler, F. Solid-State NMR Investigation of the Possible Existence of "Nanoblocks" in the Clear Solution Synthesis of MFI Materials. *J. Phys. Chem. C* **2008**, *112*, 80−88.

(22) Follens, L. R.; Aerts, A.; Haouas, M.; Caremans, T. P.; Loppinet, B.; Goderis, B.; Vermant, J.; Taulelle, F.; Martens, J. A.; Kirschhock, C. E. A. Characterization of Nanoparticles in Diluted Clear Solutions for Silicalite-1 Zeolite Synthesis Using Liquid 29Si NMR, SAXS and DLS. *Phys. Chem. Chem. Phys.* **2008**, *10*, 5574.

(23) Bell, R. G.; Lewis, D. W.; Voigt, P.; Freeman, C. M.; Thomas, J. M.; Catlow, C. R. A. Computer Modelling of Sorbates and Templates in Microporous Materials. *Stud. Surf. Sci. Catal.* **1994**, *84*, 2075−2082.

(24) Burchart, E. D. V.; VanKoningsveld, H.; VandeGraaf, B. Molecular Mechanics Studies of TBA and TPA in MEL and MFI. *Microporous Mater.* **1997**, *8*, 215−222.

(25) Trofymluk, O.; Levchenko, A. A.; Navrotsky, A. Mesoporous Silica Synthesis: Energetics of Interaction between Framework and

DOI: 10.1021/acs.jpcc.8b08251
J. Phys. Chem. C 2019, 123, 5326−5335

Structure Directing Agent. *Microporous Mesoporous Mater.* **2012**, *149*, 119−125.
(26) Kirschhock, C. E. A.; Ravishankar, R.; Verspeurt, F.; Grobet, P. J.; Jacobs, P. A.; Martens, J. A. Identification of Precursor Species in the Formation of MFI Zeolite in the TPAOH−TEOS−H_2O System. *J. Phys. Chem. B* **1999**, *103*, 4965−4971.
(27) Kirschhock, C. E. a; Ravishankar, R.; Jacobs, Pa.; Martens, Ja. Aggregation Mechanism of Nanoslabs with Zeolite MFI-Type Structure. *J. Phys. Chem. B* **1999**, *103*, 11021−11027.
(28) Liang, D.; Follens, L. R. A.; Aerts, A.; Martens, J. A.; Van Tendeloo, G.; Kirschhock, C. E. A. TEM Observation of Aggregation Steps in Room-Temperature Silicalite-1 Zeolite Formation. *J. Phys. Chem. C* **2007**, *111*, 14283−14285.
(29) Nikolakis, V.; Kokkoli, E.; Tirrell, M.; Tsapatsis, M.; Vlachos, D. G. Zeolite Growth by Addition of Subcolloidal Particles: Modeling and Experimental Validation. *Chem. Mater.* **2000**, *12*, 845−853.
(30) Davis, T. M.; Drews, T. O.; Ramanan, H.; He, C.; Dong, J.; Schnablegger, H.; Katsoulakis, Ma.; Kokkoli, E.; McCormick, A. V.; Penn, R. L.; et al. Mechanistic Principles of Nanoparticle Evolution to Zeolite Crystals. *Nat. Mater.* **2006**, *5*, 400−408.
(31) Ohsuna, T.; Terasaki, O.; et al. Electron Microscopic Study of Intergrowth of MFI and MEL: Crystal Faults in B-MEL. *J. Phys. Chem. B* **1997**, *101*, 9881−9885.
(32) Vilaseca, M.; Mateo, E.; Palacio, L.; Prádanos, P.; Hernández, A.; Paniagua, A.; Coronas, J.; Santamaría, J. AFM Characterization of the Growth of MFI-Type Zeolite Films on Alumina Substrates. *Microporous Mesoporous Mater.* **2004**, *71*, 33−37.
(33) Lupulescu, A. I.; Rimer, J. D. In Situ Imaging of Silicalite-1 Surface Growth Reveals the Mechanism of Crystallization. *Science* **2014**, *344*, 729−732.
(34) Piccione, P. M.; Yang, S. Y.; Navrotsky, A.; Davis, M. E. Thermodynamics of Pure-Silica Molecular Sieve Synthesis. *J. Phys. Chem. B* **2002**, *106*, 3629.
(35) Yang, S.; Navrotsky, A. In Situ Calorimetric Study of the Growth of Silica TPA-MFI Crystals from an Initially Clear Solution. *Chem. Mater.* **2002**, *14*, 2803−2811.
(36) Yang, S.; Navrotsky, A. Early-Stage Reactions in Synthesis of TPA-Silicalite-1: Studies by in Situ Calorimetry, SAXS, and pH Measurements. *Chem. Mater.* **2004**, *16*, 3682−3687.
(37) Rimer, J. D.; Trofymluk, O.; Navrotsky, A.; Lobo, R. F.; Vlachos, D. G. Kinetic and Thermodynamic Studies of Silica Nanoparticle Dissolution. *Chem. Mater.* **2007**, *19*, 4189−4197.
(38) Knight, C. T. G.; Wang, J.; Kinrade, S. D. Do Zeolite Precursor Species Really Exist in Aqueous Synthesis Media? *Phys. Chem. Chem. Phys.* **2006**, *8*, 3099−3103.
(39) Knight, C. T. G.; Kinrade, S. D. Comment on "Identification of Precursor Species in the Formation of MFI Zeolite in the TPAOH−TEOS−H_2O System.". *J. Phys. Chem. B* **2002**, *106*, 3329−3332.
(40) Schoeman, B. J. Analysis of the Nucleation and Growth of TPA-Silicalite-1 at Elevated Temperatures with the Emphasis on Colloidal Stability. *Microporous Mesoporous Mater.* **1998**, *22*, 9−22.
(41) Schoeman, B. J.; Regev, O. A Study of the Initial Stage in the Crystallization of TPA-Silicalite-1. *Zeolites* **1996**, *17*, 447−456.
(42) Schoeman, B. J. A High Temperature in Situ Laser Light-Scattering Study of the Initial Stage in the Crystallization of TPA-Silicalite-1. *Zeolites* **1997**, *18*, 97−105.
(43) Mores, D.; Stavitski, E.; Kox, M. H. F.; Kornatowski, J.; Olsbye, U.; Weckhuysen, B. M. Space- And Time-Resolved in-Situ Spectroscopy on the Coke Formation in Molecular Sieves: Methanol-to-Olefin Conversion over H-ZSM-5 and H-SAPO-34. *Chem. - Eur. J.* **2008**, *14*, 11320−11327.
(44) Choi, M.; Na, K.; Kim, J.; Sakamoto, Y.; Terasaki, O.; Ryoo, R. Stable Single-Unit-Cell Nanosheets of Zeolite MFI as Active and Long-Lived Catalysts. *Nature* **2009**, *461*, 246−249.
(45) Wu, L.; Degirmenci, V.; Magusin, P. C. M. M.; Lousberg, N. J. H. G. M.; Hensen, E. J. M. Mesoporous SSZ-13 Zeolite Prepared by a Dual-Template Method with Improved Performance in the Methanol-to-Olefins Reaction. *J. Catal.* **2013**, *298*, 27−40.
(46) Zhu, X.; Rohling, R.; Filonenko, G.; Mezari, B.; Hofmann, J. P.; Asahina, S.; Hensen, E. J. M. Synthesis of Hierarchical Zeolites Using an Inexpensive Mono-Quaternary Ammonium Surfactant as Mesoporogen. *Chem. Commun.* **2014**, *50*, 14658−14661.
(47) Zhang, X.; Liu, D.; Xu, D.; Asahina, S.; Cychosz, K. A.; Agrawal, K. V.; Al Wahedi, Y.; Bhan, A.; Al Hashimi, S.; Terasaki, O.; et al. Synthesis of Self-Pillared Zeolite Nanosheets by Repetitive Branching. *Science* **2012**, *336*, 1684−1687.
(48) Roth, W. J.; Nachtigall, P.; Morris, R. E.; Jir, C. Two-Dimensional Zeolites: Current Status and Perspectives. *Chem. Rev.* **2014**, 4807.
(49) Zhu, X.; Goesten, M. G.; Koekkoek, A.; Mezari, B.; Filonenko, G.; Friedrich, H.; Rohling, R.; Szyja, B. M.; Gascon, J.; Kapteijn, F.; et al. Establishing Hierarchy: The Chain of Events Leading to the Formation of Silicalite-1 Nanosheets. *Chem. Sci.* **2016**, *7*, 6506−6513.
(50) Zhang, X. Q.; Trinh, T. T.; Van Santen, R. A.; Jansen, A. P. J. Mechanism of the Initial Stage of Silicate Oligomerization. *J. Am. Chem. Soc.* **2011**, *133*, 6613−6625.
(51) Kinrade, S. D.; Knight, C. T. G.; Pole, D. L.; Syvitski, R. T. Silicon-29 NMR Studies of Tetraalkylammonium Silicate Solutions. 1. Equilibria, ^{29}Si Chemical Shifts, and ^{29}Si Relaxation. *Inorg. Chem.* **1998**, *37*, 4278−4283.
(52) Brinker, C. J. Hydrolysis and Condensation of Silicates: Effects on Structure. *J. Non-Cryst. Solids* **1988**, *100*, 31−50.
(53) Rao, N. Z.; Gelb, L. D. Molecular Dynamics Simulations of the Polymerization of Aqueous Silicic Acid and Analysis of the Effects of Concentration on Silica Polymorph Distributions, Growth Mechanisms, and Reaction Kinetics. *J. Phys. Chem. B* **2004**, *108*, 12418−12428.
(54) Chien, S. C.; Auerbach, S. M.; Monson, P. A. Modeling the Self-Assembly of Silica-Templated Nanoparticles in the Initial Stages of Zeolite Formation. *Langmuir* **2015**, *31*, 4940−4949.
(55) Ciantar, M.; Mellot-Draznieks, C.; Nieto-Draghi, C. A Kinetic Monte Carlo Simulation Study of Synthesis Variables and Diffusion Coefficients in Early Stages of Silicate Oligomerization. *J. Phys. Chem. C* **2015**, *119*, 28871−28884.
(56) Kirschhock, C. E. A.; Kremer, S. P. B.; Grobet, P. J.; Jacobs, P. A.; Martens, J. A. New Evidence for Precursor Species in the Formation of MFI Zeolite in the in the Tetrapropylammonium Hydroxide - Tetraethyl Orthosilicate - Water System. *J. Phys. Chem. B* **2002**, *106*, 4897−4900.
(57) Kumar, S.; Penn, R. L.; Tsapatsis, M. On the Nucleation and Crystallization of Silicalite-1 from a Dilute Clear Sol. *Microporous Mesoporous Mater.* **2011**, *144*, 74−81.
(58) Kumar, S.; Wang, Z.; Penn, R. L.; Tsapatsis, M. A Structural Resolution Cryo-TEM Study of the Early Stages of MFI Growth. *J. Am. Chem. Soc.* **2008**, *130*, 17284−17286.
(59) Kirschhock, C. E. A.; Ravishankar, R.; Looveren, L. Van; Jacobs, P. A.; Martens, J. A. Mechanism of Transformation of Precursors into Nanoslabs in the Early Stages of MFI and MEL Zeolite Formation from TPAOH−TEOS−H_2O and TBAOH−TEOS−H_2O Mixtures. *J. Phys. Chem. B* **1999**, *103*, 4972−4978.
(60) Szyja, B. M.; Hensen, E. J. M.; Van Santen, R. A. Retro-Analysis of Silicate Aggregation in Pentasil Zeolite Formation. *Catal. Today* **2011**, *169*, 156−166.
(61) Sun, H.; Rigby, D. Polysiloxanes: Ab Initio Force Field and Structural, Conformational and Thermophysical Properties. *Spectrochim. Acta, Part A* **1997**, *53*, 1301−1323.
(62) Rigby, D.; Sun, H.; Eichinger, B. E. Computer Simulations of Poly(ethylene Oxide): Force Field, Pvt Diagram and Cyclization Behaviour. *Polym. Int.* **1997**, *44*, 311−330.
(63) Sun, H. COMPASS: An Ab Initio Force-Field Optimized for Condensed-Phase ApplicationsOverview with Details on Alkane and Benzene Compounds. *J. Phys. Chem. B* **1998**, *102*, 7338−7364.
(64) Sun, H.; Ren, P.; Fried, J. R. The COMPASS Force Field: Parameterization and Validation for Phosphazenes. *Comput. Theor. Polym. Sci.* **1998**, *8*, 229−246.

DOI: 10.1021/acs.jpcc.8b08251
J. Phys. Chem. C 2019, 123, 5326−5335

(65) Bunte, S. W.; Sun, H. Molecular Modeling of Energetic Materials: The Parameterization and Validation of Nitrate Esters in the COMPASS Force Field. *J. Phys. Chem. B* **2000**, *104*, 2477−2489.
(66) McQuaid, M. J.; Sun, H.; Rigby, D. Development and Validation of COMPASS Force Field Parameters for Molecules with Aliphatic Azide Chains. *J. Comput. Chem.* **2004**, *25*, 61−71.
(67) Zhao, L.; Liu, L.; Sun, H. Semi-Ionic Model for Metal Oxides and Their Interfaces with Organic Molecules. *J. Phys. Chem. C* **2007**, *111*, 10610−10617.
(68) Sun, H. Ab Initio Calculations and Force Field Development for Computer Simulation of Polysilanes. *Macromolecules* **1995**, *28*, 701−712.
(69) Park, W.; Yu, D.; Na, K.; Jelfs, K. E.; Slater, B.; Sakamoto, Y.; Ryoo, R. Hierarchically Structure-Directing Effect of Multi-Ammonium Surfactants for the Generation of MFI Zeolite Nanosheets. *Chem. Mater.* **2011**, *23*, 5131−5137.
(70) Davis, M. E.; Lobo, R. F. Zeolite and Molecular Sieve Synthesis. *Chem. Mater.* **1992**, *4*, 756−768.
(71) Meng, L.; Mezari, B.; Goesten, M. G.; Hensen, E. J. M. One-Step Synthesis of Hierarchical ZSM-5 Using Cetyltrimethylammonium as Mesoporogen and Structure-Directing Agent. *Chem. Mater.* **2017**, *29*, 4091−4096.
(72) Terasaki, O.; Ohsuna, T.; Sakuma, H.; Watanabe, D.; Nakagawa, Y.; Medrud, R. C. Direct Observation of "Pure MEL Type" Zeolite. *Chem. Mater.* **1996**, *8*, 463−468.
(73) Shen, Y.; Le, T. T.; Li, R.; Rimer, J. D. Optimized Synthesis of ZSM-11 Catalysts Using 1,8-Diaminooctane as a Structure-Directing Agent. *ChemPhysChem* **2018**, *19*, 529−537.
(74) Mintova, S.; Petkov, N.; Karaghiosoff, K.; Bein, T. Crystallization of Nanosized MEL-Type Zeolite from Colloidal Precursors. *Mater. Sci. Eng., C* **2002**, *19*, 111−114.

DOI: 10.1021/acs.jpcc.8b08251
J. Phys. Chem. C 2019, 123, 5326−5335